Influence of drying conditions on layer porosity in fluidized bed spray granulation

C. Rieck [a,*], T. Hoffmann [a], A. Bück [a], M. Peglow [b], E. Tsotsas [a]

[a] Thermal Process Engineering, Otto von Guericke University, Universitätsplatz 2, 39106 Magdeburg, Germany
[b] IPT Pergande GmbH, Wilfried-Pergande-Platz 1, 06369 Weißandt-Gölzau, Germany

ABSTRACT

Particle coating experiments were performed in a lab-scale fluidized bed with varying process parameters, such as spraying rate and air inlet temperature, leading to different drying conditions. Porous (γ-Al_2O_3) and non-porous (glass) initial particles were sprayed with a sodium benzoate solution. For each experiment, the particle size distribution as well as the layer porosity was measured. The results show a dependency of the layer porosity on the drying conditions, represented by the drying potential of the fluidization gas. The obtained relationship is expressed as a linear correlation, which can be used in process models. Apart from the experimental results, a model based on population balances and heat and mass balances is presented. Simulations performed using the obtained empirical correlation are in good agreement with experimental data.

© 2014 Elsevier B.V. All rights reserved.

1. Introduction

Particle formulation in fluidized beds includes several sub-processes, such as agglomeration, layering granulation, and coating, which are widely investigated in the literature, e.g. Heinrich et al. [1], Hemati et al. [2], Hede et al. [3], Terrazas-Velarde et al. [4], Dernedde et al. [5], and Li et al. [6]. In these processes, a liquid, containing solid material, is sprayed into a fluidized bed. In the case of agglomeration, the particles collide randomly and stick together by forming liquid bridges at wet spots created by deposited droplets. Due to evaporation, solidified bridges are created. The resulting agglomerates consequently consist of several primary particles. In the case of layering granulation and coating, the dried droplets form a solid shell around the initial particle. Ideally, no agglomerates are formed. The material of the initial particle and the added solid material are the same in granulation, while, in coating, the materials are different. Additionally, a coating layer is relatively thin compared to the particle size, see e.g. Bück et al. [7].

In this work, fluidized bed coating will be treated. This process is widely used in the industry to produce pharmaceuticals, cosmetics, fertilizers, or foods. Applications may be the coating of pharmaceuticals and fertilizers to control the duration and the point of release of active substances, see, e.g. Turton [8], taste and odor masking purposes and obtaining a certain shape or surface structure, e.g. Guignon et al. [9]. In the food industry, coating can be used to separate ingredients from

their environment (water, acid, oxygen), if it is detrimental to the uncoated material, see, e.g. Werner et al. [10].

An important product property is the particle size distribution, which influences, e.g., the flow behavior and consequently the handling of the product. If the aim is to shield an active ingredient with a coating layer, the size of the product particle also affects the performance of the product, since the dissolution characteristics depend on the thickness of the coating layer. Additionally, the morphology of the coating (surface structure, porosity) will alter the dissolution behavior and therefore the release times of active substances shielded by the coating. The coating morphology has been investigated in the literature so far only in terms of the surface structure. Dewettinck et al. [11] investigated the agglomeration tendency during fluidized bed coating and performed coating experiments with different materials. They used glass beads as core material and locust bean gum, sodium alginate, carboxylmethycellulose, and κ-carrageenan as coating material. They also investigated the coating morphology by scanning electron microscope images and found differences in the surface structure. In their case, coatings consisting of locust bean gum and κ-carrageenan appeared to be very smooth and non-porous, whereas coatings consisting of the other materials showed imperfections and surface roughness. Tzika et al. [12] investigated the influence of process variables (e.g. spraying rate and fluidization air velocity) on the morphology and quality of a latex coating of fertilizer seeds in a Wurster fluidized bed. The coated particles were examined by scanning electron microscope images and the release rates of the nutrients were measured. By changing the spraying rate, the drying conditions in the fluidized bed were also varied automatically. The results show an influence of the spraying rate on the surface structure of the

* Corresponding author. Tel.: +49 391 67 12319; fax: +49 391 67 18265.
E-mail address: Christian.Rieck@ovgu.de (C. Rieck).

coating layer and also on the release rates. Hede et al. [13] also analyzed the coating morphology for scale-up purposes via scanning electron microscope images. The coating layer porosity was not part of the studies in those publications.

As stated by Tsotsas [14], it is conventionally assumed that the coating layer is compact. In fact, it is possible to produce compact layers, but they can also be porous depending on the drying conditions, namely the liquid flow rate and the gas temperature, in the fluidized bed. In the case of a porous coating layer, particles grow faster than particles with a compact layer, since a larger part of the added volume is void. This means basically that the drying conditions influence the growth kinetics of the particles, which has not been considered in modeling yet.

In publications addressing the modeling of coating and layering processes, e.g., Heinrich et al. [1], Ronsse et al. [15], Hede et al. [3] and Silva et al. [16], the enhancement of growth due to a developing porosity has not been taken into account. There are publications, e.g. Ronsse et al. [15] and Hede et al. [3], where the heat and mass transfer is modeled along with the particle growth. But these models are coupled in only one direction, i.e. particle growth influences the drying conditions but not vice versa.

This work deals with the determination of the coating layer porosity and its dependency on the drying conditions in fluidized bed spray granulation. Therefore we use the following approach:

1. determination of a semi-empirical relationship between the drying conditions and the coating layer porosity based on fluidized bed coating experiments and micro-tomography measurements;
2. development of a model based on population balance equations for the particle growth considering the coating layer porosity;
3. comparison of calculated and measured particle size distributions and evaluation of the model.

2. Experimental work

2.1. Laboratory plant

The fluidized bed coating experiments in this study were performed in a laboratory-scale plant from the Glatt company (type GPCG 1.1), which is shown in Fig. 1. In this experimental plant, only batch processes can be realized. The fluidized bed chamber is cylindrical and has a diameter of 150 mm and a height of 450 mm. The gas distributor plate, having a mean pore size of 100 μm, is made of sintered metal to achieve uniform fluidization conditions.

Sodium benzoate was used as coating material in all experiments. It is sprayed in the form of an aqueous solution into the process chamber with a two-fluid nozzle (Schlick, type 970/0 S4), which can be placed in top-spray or in bottom-spray position. The liquid is dosed by a precision metering pump (Labortechnik Sewald, type: LDP-31) and the amount of

injected liquid is detected by weighing of the supply tank. The plant operates with compressed air, which is taken from the local compressed air network. In this way, constant values for the mass flow rate of the fluidization gas and the inlet moisture content can be obtained. The measurement of the inlet and outlet gas moisture content is realized by means of infrared spectroscopy (Rosemount Analytical, type NGA 2000). To ensure constant measurement conditions, several control valves, which guarantee constant air pressure and air flow, are installed. The mass flow of fluidization gas is measured by a mass flow meter (Bronkhorst Mättig, type: F-112AC) and controlled by a throttle valve. Additionally, the gas temperatures at the inlet and outlet were measured. The electric heater allows a maximum temperature of 100 °C for the inlet gas. The plant has a built-in textile filter for the exhaust air, which has a mean pore size of 7 μm.

2.2. Experimental series

Two experimental series with different particle systems (porous and non-porous) were carried out to investigate the influence of different gas inlet temperatures and spraying rates on the particle growth and the layer porosity. Four experiments were performed in each series. All of them were run in batch mode with top-spray configuration in the fluidized bed spray granulator described.

In the first experimental series (experiments numbered from 1 to 4), glass beads with a mean particle diameter of 0.50 mm, a standard deviation of 0.058 mm and a particle density of 2400 kg/m^3 were used. This material has a high sphericity of 0.94, which is close to the model assumption of spherical particles. In addition, the glass beads are non-porous, so during the granulation no droplet imbibition occurs. In the first experimental series, four experiments were performed in which the gas inlet temperature (from 50 °C to 95 °C) and the spraying rate (500 g/h to 1100 g/h) were varied. The specific process parameters of each experiment are listed in Table 1. All other process parameters, such as initial bed mass (1 kg), the amount of sprayed solution (1 kg), mass flow rate of the gas (120 kg/h), and concentration (30 ma-%) of the injected solution are the same for all experiments of the series. The time of the experiments varied between 55 and 120 min, due to the spraying rate and fixed amount of sprayed material.

In the second experimental series (experiments numbered from 5 to 8), porous and hygroscopic γ-Al$_2$O$_3$ particles, having a mean diameter of 0.61 mm, a standard deviation of 0.016 mm, and a particle density of 1280 kg/m^3, were used. The sphericity of the particles is 0.97. The process parameters of the second series correspond exactly to those of the first series, except for the mass flow rate of the gas and the initial bed mass. Because of the smaller density of the γ-Al$_2$O$_3$ particles, these values have been adjusted to 75 kg/h and 0.5 kg to maintain a similar fluidization regime as in the first series.

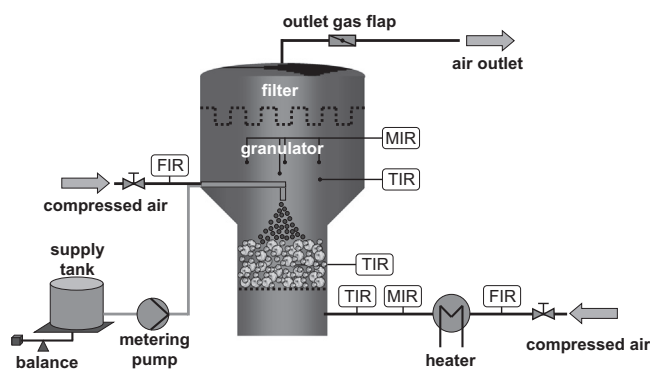**Fig. 1.** Scheme and photo of the experimental plant used in this study.

No.	Material	t_{end}	$\vartheta_{g,inlet}$	$\vartheta_{g,outlet}$	$\dot{M}_{sus}$	$\dot{M}_g$	Y_{inlet}	Y_{outlet}	Y_{sat}
		[s]	[°C]	[°C]	[g/h]	[kg/h]	[kg/kg]	[kg/kg]	[kg/kg]
1	Glass	7148	50	40.8	504	120	0.0010	0.0035	0.0127
2	Glass	3722	50	34.1	967	120	0.0010	0.0061	0.0127
3	Glass	7026	95	80.8	512	120	0.0010	0.0036	0.0246
4	Glass	2820	95	70.1	1277	120	0.0010	0.0076	0.0244
5	γ-Alumina	7184	50	37.0	501	75	0.0010	0.0056	0.0131
6	γ-Alumina	3210	50	25.2	1121	75	0.0010	0.0109	0.0135
7	γ-Alumina	7206	95	80.0	500	75	0.0010	0.0053	0.0257
8	γ-Alumina	3320	95	65.4	1084	75	0.0010	0.0106	0.0254

At the end of each experiment, a product sample was taken from the fluidized bed chamber and the particle size distribution was determined offline using a particle size analyzer (Retsch GmbH, type: Camsizer). Additionally, scanning electron microscope images (Phenom-World BV, type: Pro Desktop SEM) of the samples were produced to gain insight into the surface structure of the particles. The porosity of the coating layer was evaluated via X-ray micro-tomography (ProCon X-ray GmbH, type: CT-ALPHA). The measurement procedure was similar as reported by Dadkhah et al. [17], who dealt with characterization of agglomerates. This method is based on different absorption properties of X-rays for different materials, which leads to images of the sample with different gray values. The sample is rotated so that from the resulting images a volume image can be reconstructed. In this volume image the core and the shell can be separated and their volumes and porosities can be calculated. Note that the shell porosity is a mean value in this case and therefore does not depend on the thickness of the shell. In the case of layering granulation, where the materials of the core particle and the coating layer are the same, additives such as potassium iodide can be added to the liquid sprayed on the particles, see Dadkhah [18]. In this way, micro-tomography can also be applied, if the materials are the same.

3. Model development

3.1. Particle growth model

Several approaches to model growth processes in fluidized beds can be found in the literature. In many publications a two-compartment model, which divides the process chamber into a spray zone and a drying zone, is used, e.g. Sherony [19], Wnukowski and Setterwall [20], Silva et al. [16], Hoffmann et al. [21], and Li et al. [6]. This is done, because the spray cone created by the nozzle covers only a volume fraction of the process chamber. Due to fluidization, a transport between the zones will occur. Maronga and Wnukowski [22] introduced a third compartment, the non-active zone, where the particles are not directly involved in the coating process, to account for the effects of stagnant regions on the particle size distribution.

In this work, a two-compartment model is used. A scheme of this compartment model is shown in Fig. 2. Particles in the spray zone are able to receive new solid material, whereas in the drying zone only particle drying occurs. The mass flow rates between these two zones depend on the mean residence time in each compartment. For each zone, one population balance equation is derived. Both equations contain the mass flow rates between the zones, whereas the growth term is only included into the equation for the spray zone, since the particles are only able to grow in this compartment.

In order to derive the population balance model, the following assumptions are made:

- The particles are spherical and their size is therefore characterized by the particle diameter x.
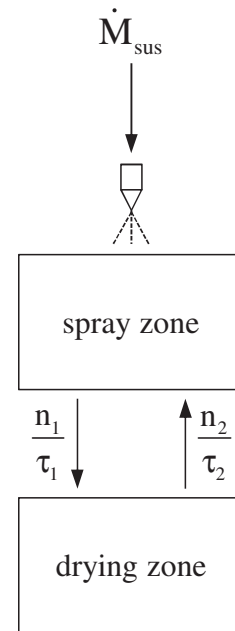- Each compartment is considered to be perfectly mixed. No external coordinates are needed.

Fig. 2. Scheme of the two compartment model used in this study. The particles in the spray zone are able to receive droplets of the atomized solution leading to layering growth, whereas particles in the drying zone are only able to dry.

- The relative size of each compartment is constant.
- Further, it is assumed that aggregation and breakage are negligible. The operating parameters in the experiments were chosen to favor rebound of colliding particles, instead of aggregation. This can be estimated by the critical Stokes number, which has been introduced by Ennis et al. [23]. Thus, only growth by layering and particle exchange between the zones need to be considered.

For only one property coordinate, which is in this case the particle diameter x, the population balance equations of the two compartments can be written as

$$\frac{\partial n_1}{\partial t} = -\frac{\partial(G n_1)}{\partial x} - \frac{n_1}{\tau_1} + \frac{n_2}{\tau_2}, \tag{1}$$

$$\frac{\partial n_2}{\partial t} = \frac{n_1}{\tau_1} - \frac{n_2}{\tau_2}, \tag{2}$$

where n_1 and n_2 denote the number density functions in the spray zone and in the drying zone. G represents the growth rate of the particles in the spray zone, τ_1 and τ_2 denote the residence times of the particles in the two zones. To ensure mass conservation of this two-compartment approach, the residence times of both zones must fulfill the following condition:

$$\frac{\tau_1}{\tau_2} = \frac{\varphi}{1-\varphi}. \tag{3}$$

In this equation, φ denotes the relative size of the spray zone in terms of a volumetric fraction and can have values between 0 and 1. This approach is also used by Maronga and Wnukowski [22], Silva et al. [16] and Hampel et al. [24]. In other publications, e.g. Sherony [19] and Wnukowski and Setterwall [20], the size of the spray zone is defined by the fraction or portion of particles inside the spray compartment, without describing, if it is a number or mass fraction of the particles. Li et al. [6] use a number fraction of the particles in the spray zone to characterize its size.

The number density function can also be expressed as the normalized number density function q_0:

$$q_0(t,x) = \frac{n(t,x)}{\mu_0(t)}. \tag{4}$$

Here, μ_0 denotes the zeroth moment of the number density distribution. A general definition of the k-th moment is given by

$$\mu_k(t) = \int_0^\infty x^k n(t,x)\mathrm{d}x. \tag{5}$$

In order to solve the set of partial differential equations, two initial conditions and one boundary condition need to be specified. At $t = 0$, the particle size is described by the initial particle size distribution $n_i(x)$. Corresponding to the relative size of the spray zone φ, the initial number density function $n_i(x)$ is distributed among the zones, which leads to the following initial conditions:

$$n_1(t = 0, x) = \varphi n_i(x), \tag{6}$$

$$n_2(t = 0, x) = (1-\varphi)n_i(x). \tag{7}$$

The initial conditions used in the simulations were adjusted to the particle size distributions of the particles, see Fig. 3. The initial number density function for the γ-Al$_2$O$_3$ particles was obtained using a Gaussian distribution with a mean diameter and a standard deviation shown in Table 2. The initial number density function of the glass particles could not be described by a normal distribution without notable deviations. Instead, a piecewise cubic Hermite interpolation method was used to approximate the measured data points.
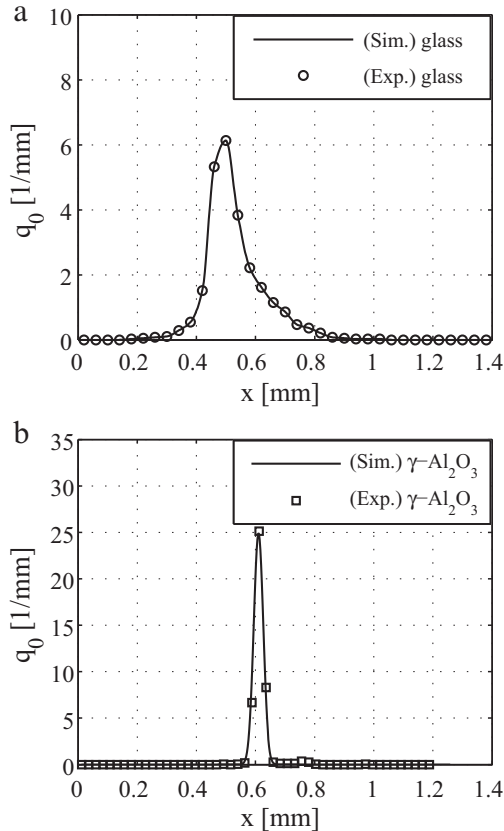

Fig. 3. Plot of the initial conditions used in the simulations.

Table 2
Mean diameter and standard deviation of the initial particle size distributions (marked with "initial") and the final particle size distributions (series 1: No. 1 to No. 4 and series 2: No. 5 to 8) as well as the calculated drying potentials and measured porosities.

No.	Material	x_m	σ	η	ε_{sh}
		[mm]	[mm]	[-]	[-]
Initial	Glass	0.4990	0.0576	–	–
1	Glass	0.6258	0.0773	0.79	0.50
2	Glass	0.6412	0.0665	0.56	0.64
3	Glass	0.6087	0.0672	0.89	0.46
4	Glass	0.6354	0.0764	0.72	0.50
Initial	γ-Al$_2$O$_3$	0.6131	0.0158	–	–
5	γ-Al$_2$O$_3$	0.7482	0.0230	0.62	0.21
6	γ-Al$_2$O$_3$	0.7693	0.0255	0.21	0.38
7	γ-Al$_2$O$_3$	0.7434	0.0249	0.83	0.18
8	γ-Al$_2$O$_3$	0.7553	0.0262	0.61	0.28

The boundary condition is set at the left boundary of the size coordinate. Since there is no nucleation considered in this model, the boundary condition equals zero:

$$(Gn_1)|_{x=0} = 0. \tag{8}$$

In the next step, a mathematical formulation for the growth kinetics G, which has to include the porosity of the formed shell as a parameter, has to be derived. In this context, G is defined as

$$G = \frac{\mathrm{d}x}{\mathrm{d}t}, \quad [G] = \mathrm{ms}^{-1}. \tag{9}$$

Here, an assumption about the distribution of the sprayed solution in the fluidized bed has to be made. Mörl et al. [25] suggest that the distribution of the liquid is directly related to the surface area of the particles, which can be calculated from the second moment μ_2 of the number density function

$$G = \frac{2\dot{M}_{sus,s}}{\varrho_s \pi \mu_2}. \tag{10}$$

This leads to a property independent growth law, which means that all particles grow with the same velocity. A more general approach is given by Hoffmann et al. [21] and Peglow et al. [26], where the liquid distribution is related to an arbitrary moment μ_j of the number density function enabling a property dependent growth law. This assumption leads to the following expression for the mass balance of a single particle:

$$\frac{\mathrm{d}M_p}{\mathrm{d}t} = \dot{M}_{sus,s}\frac{x^j}{\mu_j}, \quad j = 0...3, \tag{11}$$

where $\dot{M}_{sus,s}$ represents the mass flow rate of the solid material. By expansion, another expression for the mass balance of a single particle can be derived:

$$\frac{\mathrm{d}M_p}{\mathrm{d}t} = \frac{\mathrm{d}M_p}{\mathrm{d}x}\frac{\mathrm{d}x}{\mathrm{d}t}. \tag{12}$$

In order to find a formulation for the mass of a single particle M_p including the porosity of the shell, the particle has to be divided into core and shell, as shown in Fig. 4. The mass of the particle is composed of the mass of the initial particle (core) and the mass of the added solid material (shell). These two masses can be expressed as

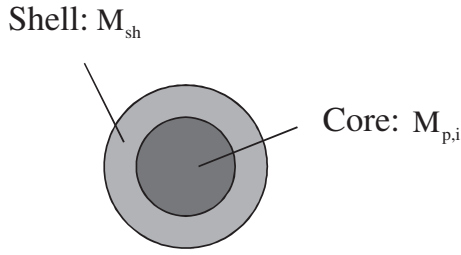$$M_{p,i} = \varrho_{p,i}V_{p,i} = \varrho_{p,i}\frac{\pi}{6}x_i^3, \tag{13}$$

Fig. 4. Segmentation of a granule into core and (porous) shell.

$$M_{sh} = \varrho_{sh}\left(V_p(t) - V_{p,i}\right) = \varrho_{sh}\frac{\pi}{6}\left(x(t)^3 - x_i^3\right). \tag{14}$$

The density of the shell ϱ_{sh} depends on the density of the added solid material ϱ_s (without any pores) and the shell porosity ε_{sh}:

$$\varrho_{sh} = \varrho_s(1 - \varepsilon_{sh}). \tag{15}$$

This leads to the following expression for the mass of a single particle:

$$M_p(t) = \frac{\pi}{6}\left(\varrho_{p,i}x_i^3 + \varrho_s(1 - \varepsilon_{sh})\left(x(t)^3 - x_i^3\right)\right). \tag{16}$$

The combination of Eqs. (9), (11), (12) and (16) yields the expression for the growth kinetics G_j including the shell porosity ε_{sh}. Eq. (17) shows that a higher porosity leads to a higher growth rate due to the adding of void volume to the particle.

$$G_j = \frac{2\dot{M}_{sus,s}}{\varrho_s\pi(1 - \varepsilon_{sh})}\frac{x^{j-2}}{\mu_j}. \tag{17}$$

The total growth rate of the particles G can then be defined as

$$G = \sum_k^N \lambda_k G_k \quad \text{with} \quad \sum_k^N \lambda_k = 1. \tag{18}$$

Due to the required mass conservation, the sum of all λ_k must equal unity. A selection of $\lambda_2 = 1$ yields the above described property independent growth law (Eq. (10)).

3.2. Drying model

Fluidized bed drying has been investigated theoretically and experimentally in the literature, e.g. Heinrich et al. [27], Wang et al. [28] and Khanali et al. [29,30]. A very accurate but complex model is given by Burgschweiger and Tsotsas [31]. It takes into account the distribution of moisture, enthalpy, and the number of the particles with respect to the residence time of the particles in the fluidized bed. In addition, the fluidized bed is divided into a suspension phase (gas phase with perfectly backmixed particles) and a particle-free bubble phase. Furthermore, heat transfer between the wall of the apparatus and the particles, the suspension phase, the bubble phase, and the environment is considered. In this work, a much simpler model is used to calculate the drying conditions (moisture and temperature of the gas and the particles). The main assumptions of this model are:

- no distinction between suspension and bubble phase,
- perfectly mixed solid phase,
- plug flow of the gas phase,
- no second drying stage.

A control volume of the fluidized bed with the considered mass, enthalpy, and heat flow rates is shown in Fig. 5. The mass of water in
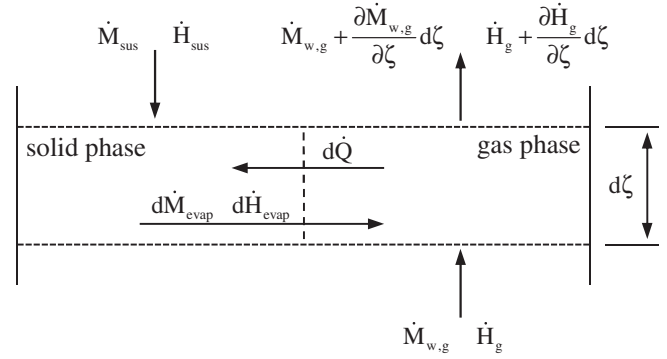

Fig. 5. Depiction of the mass, enthalpy, and heat flow rates in a control volume.

the solid phase $M_{w,p}$ depends on the mass flow rate of the liquid $\dot{M}_{sus,l}$ and also on the drying rate $\dot{M}_{evap}$. Due to the assumption of a perfectly mixed solid phase, no spatial position of the particles has to be considered, which gives an ordinary differential equation for the change of the water mass in the solid phase:

$$\frac{dM_{w,p}}{dt} = -\dot{M}_{evap} + \dot{M}_{sus,l}. \tag{19}$$

Due to the assumption of plug flow in the gas phase, the mass of water in the gas phase depends on the spatial coordinate, which is in this case scaled with the total height of the bed L_{bed} to get a dimensionless spatial coordinate ζ. The mass balance for the gas phase yields the following partial differential equation:

$$\frac{\partial M_{w,g}}{\partial t} = -\frac{\partial \dot{M}_{w,g}}{\partial \zeta} + d\dot{M}_{evap}. \tag{20}$$

The moisture content of the solid phase X and the gas phase Y is calculated from the mass of water and the mass of dry matter in each phase. The mass of dry particles in the bed can be calculated from the third moment of the number density function in the bed. The mass of dry gas is calculated from the volume of the bed and the bed porosity, which can be calculated from correlations given by Richardson and Zaki [32] and Martin [33].

$$X = \frac{M_{w,p}}{M_{p,dry}}, \quad M_{p,dry} = \varrho_p\frac{\pi}{6}\int_0^\infty x^3 n\,dx \tag{21}$$

$$Y = \frac{M_{w,g}}{M_{g,dry}}, \quad M_{g,dry} = \varepsilon_{bed}\varrho_g\frac{\pi}{4}d_{bed}^2 L_{bed}. \tag{22}$$

The drying rate is calculated from Eq. (23), where β is the mass transfer coefficient, A_{bed} is the total surface of the particles in the fluidized bed, Y_{sat} is the moisture content of the gas at saturation, and Y is the moisture content of the bulk of the gas stream:

$$\dot{M}_{evap} = \varrho_g\beta A_{bed}(Y_{sat} - Y). \tag{23}$$

The saturation moisture content Y_{sat} is the maximum amount of liquid that can be absorbed by the gas at a certain temperature. It is calculated from:

$$Y_{sat} = 0.622\frac{P_{sat}}{P - P_{sat}}, \quad P_{sat} = \exp\left(A^* - \frac{B^*}{C^* + \vartheta_{g,sat}}\right). \tag{24}$$

The empirical Antoine constants $A^* = 23.621$, $B^* = 4065\,°C$ and $C^* = 236.2506\,°C$ are taken from Glück [34]. In Eq. (24), $\vartheta_{g,sat}$ represents
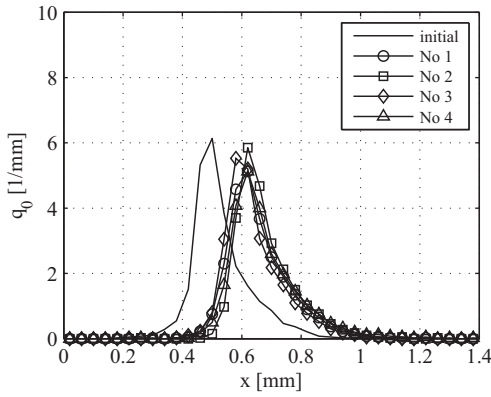
Fig. 6. Depiction of the measured particle size distributions for experiments No. 1 to No. 4 (core material: glass beads). In this picture, the initial particle size distribution as well as the particle size distributions at the end of each experiment are shown.
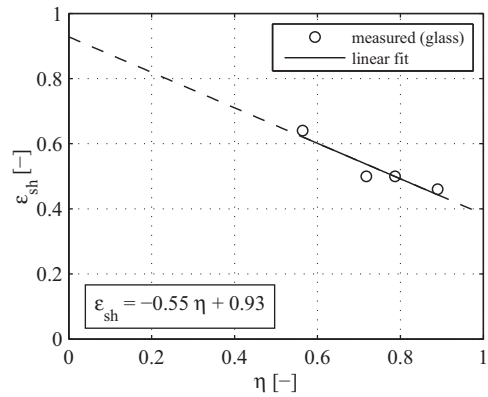

Fig. 8. Depiction of the measured dependency of the shell porosity on the drying potential for non-porous glass beads coated with sodium benzoate. Additionally a linear correlation is plotted, which was obtained via linear least squares method.

the gas temperature at adiabatic saturation, which is calculated iteratively:

$$\vartheta_{g,inlet} - \vartheta_{g,sat} = \frac{\Delta h_{evap} + (c_v - c_w)\vartheta_{g,sat}}{c_g + Y_{inlet}c_v}(Y_{sat} - Y_{inlet}).$$ (25)

Here, Δh_{evap} denotes the evaporation enthalpy at 0 °C and c_v, c_w, and c_g denote the specific heat capacities of vapor, water, and the fluidization gas. The variables Y_{inlet} and $\vartheta_{g,inlet}$ represent the inlet moisture content and inlet temperature of the gas.

The enthalpy of the solid phase depends on the enthalpy flow rate $\dot{H}_{evap}$ leaving the solid phase due to the evaporation of the water, the enthalpy flow rate $\dot{H}_{sus}$ entering the solid phase due to liquid spraying, and

on the heat flow rate $\dot{Q}$, which is exchanged between both phases. The following ordinary differential equation is derived:

$$\frac{dH_p}{dt} = -\dot{H}_{evap} + \dot{H}_{sus} + \dot{Q}.$$ (26)

The enthalpy of the gas phase depends also on the enthalpy flow rate due to evaporation and on the heat flow rate. Additionally, the enthalpy transport due to convection is considered. The balance yields:

$$\frac{\partial H_g}{\partial t} = -\frac{\partial \dot{H}_g}{\partial \zeta} + d\dot{H}_{evap} - d\dot{Q}.$$ (27)
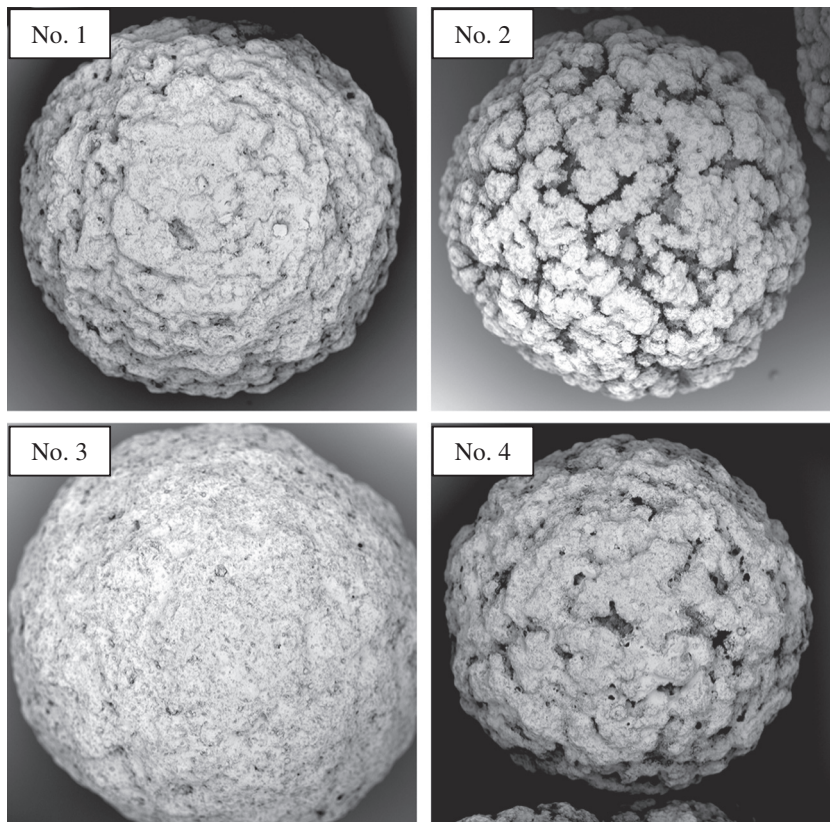

Fig. 7. Scanning electron microscope images of the glass beads coated with sodium benzoate. Depending on the drying conditions the coating layer can be porous or compact.
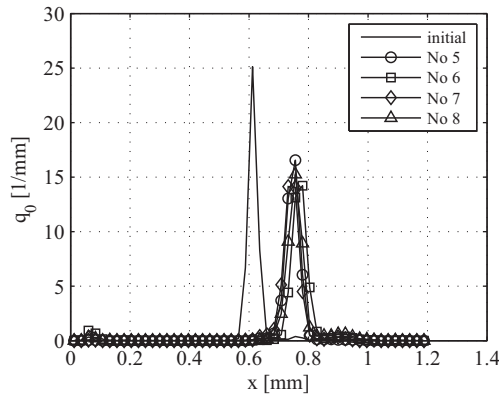
Fig. 9. Depiction of the measured particle size distributions for experiments No. 5 to No. 8 (core material: γ-Al₂O₃ particles). In this picture, the initial particle size distribution as well as the particle size distributions at the end of each experiment is shown.

In order to calculate the temperatures of each phase from the corresponding enthalpy content, the following equations are used:

$$H_p = M_{p,dry}\vartheta_p\left(c_p + Xc_w\right),\tag{28}$$

$$H_g = M_{g,dry}\left(c_g\vartheta_g + Y\left(c_v\vartheta_g + \Delta h_{evap}\right)\right).\tag{29}$$

The abovementioned enthalpy and heat flow rates $\dot{Q}$, $\dot{H}_{evap}$, and $\dot{H}_{sus}$ are calculated from:

$$\dot{Q} = \alpha A_{bed}\left(\vartheta_g - \vartheta_p\right),\tag{30}$$

$$\dot{H}_{evap} = \dot{M}_{evap}\left(c_v\vartheta_p + \Delta h_{evap}\right),\tag{31}$$

$$\dot{H}_{sus} = \dot{M}_{sus}\left(w_s c_w + (1-w_s)c_p\right)\vartheta_{sus}.\tag{32}$$

In these equations, α denotes the heat transfer coefficient, w_s denotes the mass fraction of solid material in the sprayed liquid and c_p represents the specific heat capacity of the particles.

To calculate the initial and boundary conditions for the gas phase, the measured values for the moisture content and the temperature of the inlet gas, shown in Table 1, were used. Note, that for the initial condition, a constant moisture and temperature profile was assumed, which means that moisture content and temperature are the same in each height element. To calculate the initial condition of the solid phase, it was assumed that the particles are dry and have the same temperature as the gas phase.

In order to link drying with the coating layer porosity, the drying potential of the fluidization gas representing the drying conditions is used. It is calculated from:

$$\eta = \frac{Y_{sat} - Y_{out}}{Y_{sat} - Y_{in}}, \quad Y_{out} = Y(\zeta = 1) = Y(L_{bed}).\tag{33}$$

If the gas is dry, the drying potential will tend towards unity. Consequently, the drying potential will be zero, if the gas is saturated. The heat and mass transfer coefficients α and β are calculated using correlations given by Groenewold and Tsotsas [35].
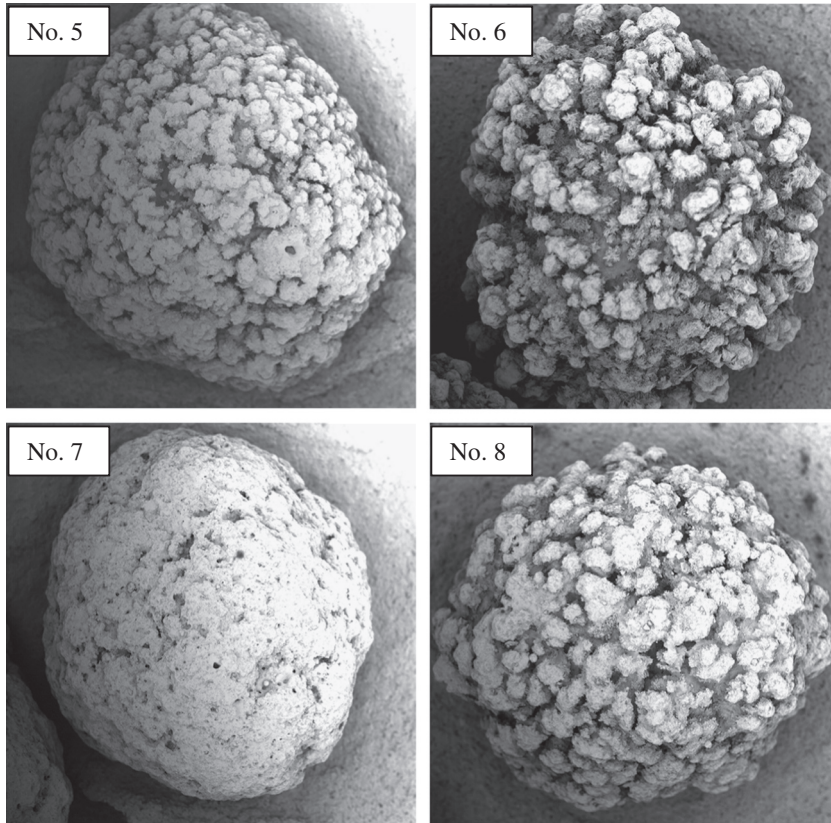

Fig. 10. Scanning electron microscope images of the γ-Al₂O₃ particles coated with sodium benzoate. They show the same principal dependency of the coating layer's structure on the drying conditions as the scanning electron microscope images of the glass particles.
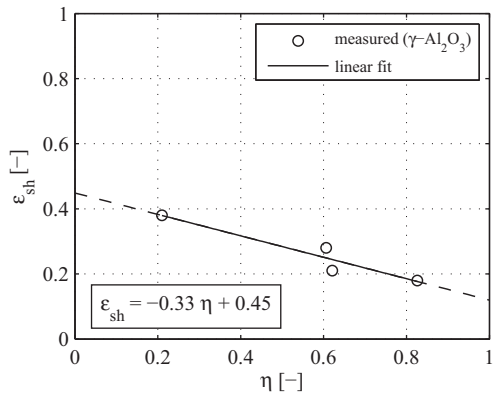
Fig. 11. Depiction of the measured dependency of the shell porosity on the drying potential for porous γ-Al$_2$O$_3$ particles coated with sodium benzoate. Additionally a linear correlation is plotted, which was obtained via linear least squares method.

4. Results

4.1. Experimental results

The process parameters of both experimental series are displayed in Table 1. In Fig. 6, the initial and final particle size distributions of the first experimental series are displayed. In Table 2, the mean diameter and the standard deviation of the initial and final particle size distributions as well as the calculated drying potentials and measured porosities are summarized. The initial size distributions were identical throughout each series. Therefore, the values of the mean diameter and standard deviation of the initial distributions are shown only once per series in Table 2 (marked with "initial"). The values of the final size distributions

are marked with the number of the experiment (series 1: No. 1 to No. 4 and series 2: No. 5 to No. 8). The increase in the mean diameter and the shift of the particle size distribution to larger diameters indicate the growth of the particles. It appears, that the particles produced in experiment No. 2 have the largest diameter, while in experiment No. 3 the smallest particles were produced.

The results of the SEM measurements are depicted in Fig. 7. They show different surface structures of the coating layer. Comparing the SEM images and the particle size distributions, it can be seen that the largest particles produced in experiment No. 2 show the most porous structure of the coating layer. The particles of experiment No. 1 and No. 4 show a similar structure, while the smallest particles (experiment No. 3) have the most compact structure of the coating layer. This indicates, that the porosity of the coating layer causes the differences in the particle sizes.

This is also confirmed by the results of the porosity measurements, shown in Table 2. Fig. 8 shows the measured porosities as a function of the drying potential, which is calculated from the measured moisture content of the gas (Eq. (33)) and the moisture content at saturation shown in Table 1. The results show, that with increasing drying potential the porosity is decreasing. That means, if the process conditions lead to a low drying potential (high moisture content, low temperature), the porosity of the formed coating layer is high. Consequently, the porosity is low, if the drying potential is high (low moisture content, high temperature). A linear expression for the porosity of the coating layer as a function of the drying potential obtained via linear least squares method is given in Fig. 8. An explanation of this behavior is given after presenting the results of the experiments in series two.

The measured particle size distributions of the second experimental series, where porous γ-Al$_2$O$_3$ particles were used, are shown in Fig. 9. The mean diameter and standard deviation of the particle size distributions are shown in Table 2. In experiments No. 5 and No. 8, particles
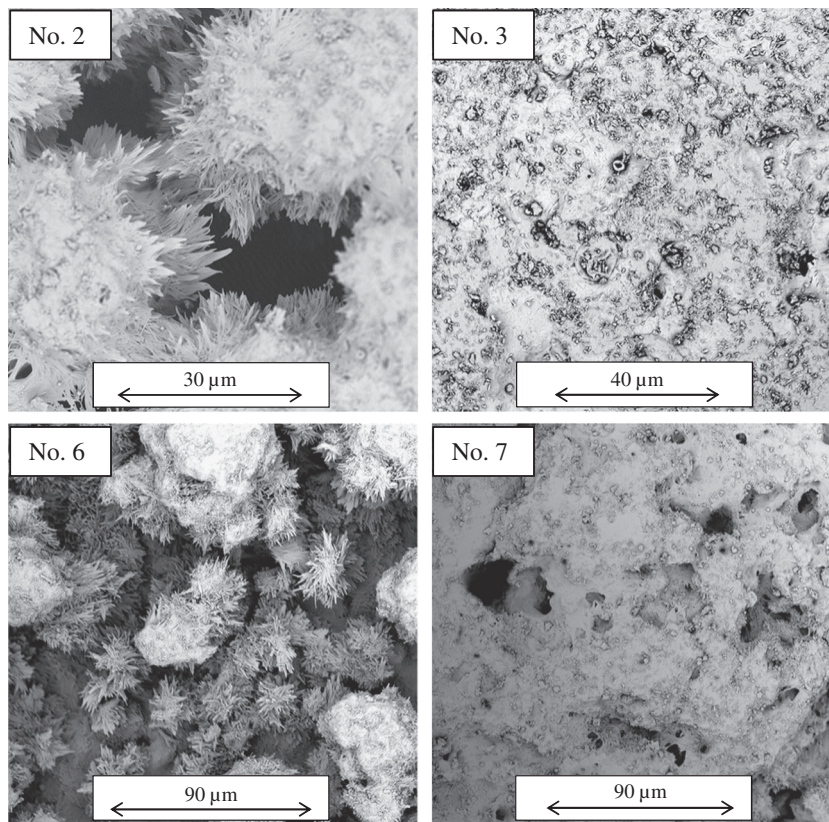

Fig. 12. Scanning electron microscope images of the glass beads and γ-Al$_2$O$_3$ particles coated with sodium benzoate.
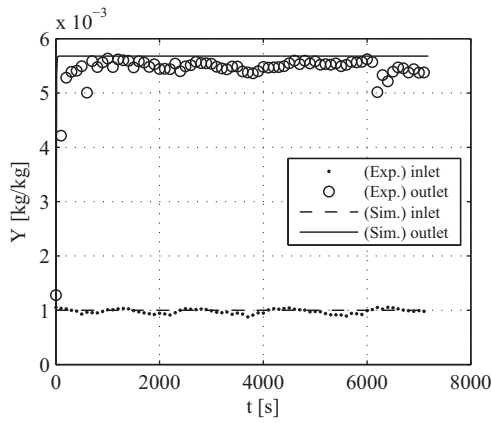
Fig. 13. Comparison between calculated and measured moisture content of the gas at the inlet and outlet of the fluidized bed for experiment No. 5.

Fig. 15. Comparison between the drying potential calculated from the measured temperatures and moisture contents and the drying potential calculated from the simulation.

with similar size distributions were produced, while the particles obtained in experiment No. 7 are the smallest and the particles produced in experiment No. 6 are the largest particles.

These particles were investigated by means of a scanning electron microscope as well. The resulting images are depicted in Fig. 10. In this case, the same behavior as in the first experimental series can be observed: large particles show a more porous structure of the coating layer, than small ones. This statement is supported by the results of the micro-tomography measurements, which are also shown in Table 2. The largest particles (experiment No. 6) have the highest porosity and the smallest particles (experiment No. 7) accordingly have the lowest porosity. Additionally, particles of similar size and surface structure (experiments No. 5 and No. 8) have similar porosities. In Fig. 11, the measured porosity values are plotted versus the corresponding drying potential. A linear expression for the relationship between the porosity of the coating layer and the drying potential is also given in Fig. 11. From this plot, the same dependency can be obtained: particles with porous coating layers are produced if the drying potential is low.

This may be due to the competing phenomena inside a droplet deposited on the particle surface: drying of the liquid and crystallization of the solid. In the case of dry conditions (high drying potential), the drying rate is high and consequently, the drying time of a droplet is small. Then, nuclei formed in the shrinking droplet may not have enough time to grow and form a porous structure. In the case of rather wet conditions (low drying potential), the drying time is greater giving the nuclei time to grow and form porous structures. In addition, the
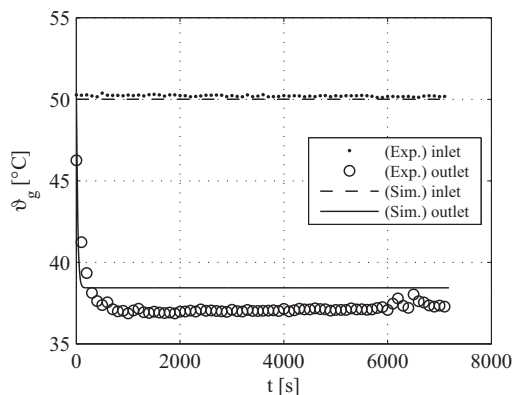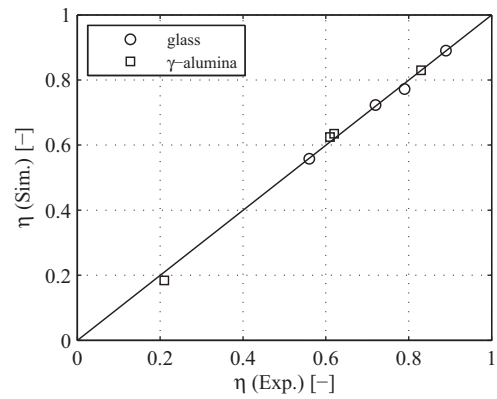
temperature in the bed may also influence the nucleation and growth kinetics of the crystals directly in both cases. An indication can be found by taking a closer look at the surface morphology in Fig. 12. The scanning electron microscope images of experiment Nos. 2 and 6 show porous structures containing needle-shaped crystals. Those particles were produced at low drying potentials and temperatures. However, the images of the particles produced at high drying potentials and temperatures (experiment Nos. 3 and 7), show no needle-shaped crystals incorporated into the structure.

The trend described above is similar for both particle systems, but the drying potentials as well as the measured porosities differ from each other leading to different empirical relations. The drying potentials are different because of the process conditions. Taking a look at Table 1 reveals that the inlet moisture content and the saturation moisture content are similar in the case of different materials, while the outlet moisture content is not. This is due to the different mass flow rates of the fluidization gas. When using γ-Al$_2$O$_3$ particles, a smaller mass flow rate was used, to enable a similar fluidization regime. This modification leads to higher outlet moisture contents and consequently changes the drying potential. Additionally, changing the mass flow rate of the fluidization gas yields lower temperatures of the outlet gas in the case of γ-Al$_2$O$_3$ particles. Because of the lower temperatures and higher moisture contents, longer drying times of the droplets are expected and larger crystals may be formed leading to a more porous structure.

4.2. Simulation results

To compare the experimental results with the derived growth model, simulation studies were performed. In order to solve Eqs. (1), (2), (20), and (27), they are discretized using a finite volume scheme in combination with a flux limiter function given by Koren [36] to reduce numerical diffusion effects. For Eqs. (19) and (26) no discretization

Fig. 14. Comparison between calculated and measured temperature of the gas at the inlet and outlet of the fluidized bed for experiment No. 5.

Table 3
Parameters used for all simulations.

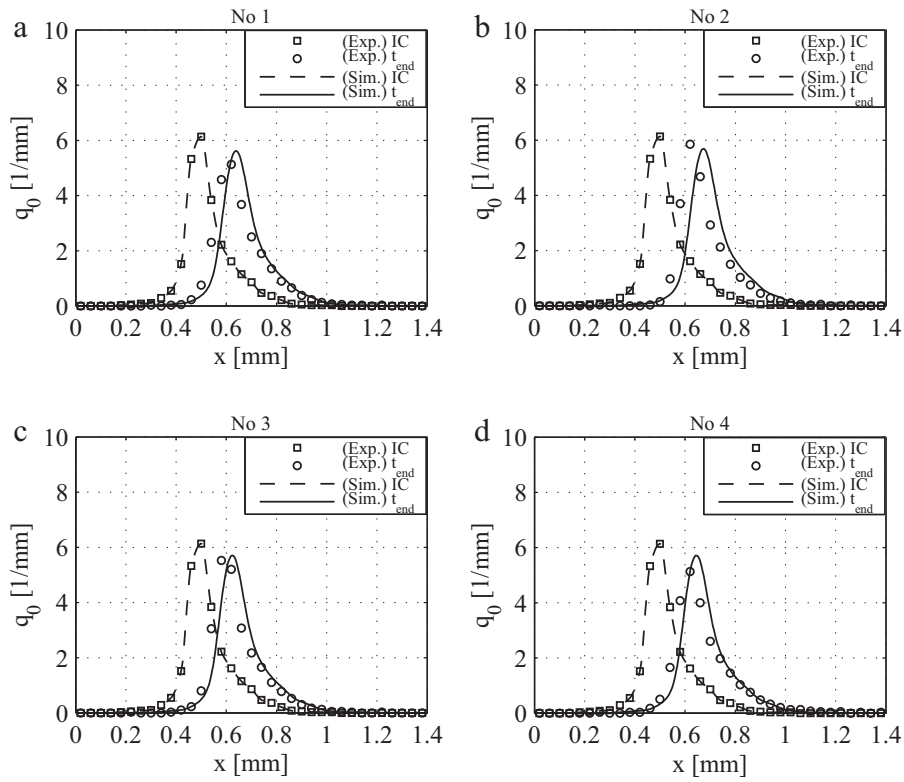| No.	φ	τ_1	η	ε_{sh}
	[–]	[s]	[–]	[–]
1	0.006	0.5	0.77	0.51
2	0.020	0.5	0.56	0.62
3	0.006	0.5	0.89	0.44
4	0.020	0.5	0.72	0.53
5	0.020	0.5	0.64	0.24
6	0.030	0.5	0.18	0.39
7	0.020	0.5	0.83	0.18
8	0.030	0.5	0.63	0.24

Fig. 16. Comparison between simulated and measured particle size distributions for the first experimental series (non-porous glass particles coated with sodium benzoate).

is needed, since they are ordinary differential equations. The numerical integration is performed using the solver ode15s provided by MATLAB Software. This solver uses numerical differentiation formulas and is suitable for stiff problems, see Shampine and Reichelt [37].

The model, which is described in Section 3, was fed with the empirical correlations shown in Fig. 8 and 11 and a simulation of each experiment was performed. First of all it was checked, if the heat and mass transfer model is able to describe the drying conditions in the fluidized
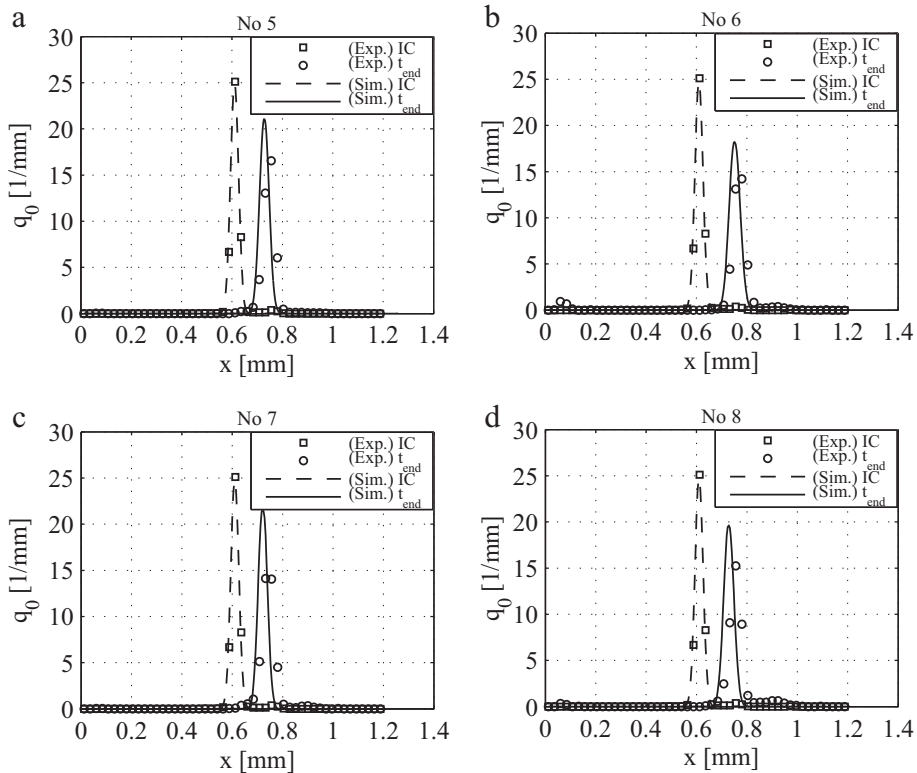

Fig. 17. Comparison between simulated and measured particle size distributions for the second experimental series (porous γ-Al₂O₃ particles coated with sodium benzoate).

bed. Therefore, moisture, temperature, and the resulting drying potential of the outlet gas obtained from both simulations and experiments are compared. In Figs. 13 and 14, the calculated moisture content and the temperature at the outlet of experiment No. 5, which is used exemplarily, are compared with experimental data. The deviations between simulation and experiment are acceptable for the purpose of calculating the drying potential. In Fig. 15, the drying potential obtained from all simulations is compared with the ones calculated from experimental data showing a prediction with good accuracy.

The parameters used for the simulations are shown in Table 3. The relative size of the spray zone φ was adjusted for each experiment due to the lack of prediction methods. It was assumed, that a small spraying rate leads to a small size of the spray zone and vice versa. The used values are in the same range as those given by Hampel et al. [24] for a spray zone in a Wurster fluidized bed. The residence time τ_1 in the spray zone is found to be in the range of 0.1 s to 0.2 s in several publications, e.g. Fries et al. [38], Hampel et al. [24], and Börner et al. [39]. In this work, a constant value of 0.5 s was used for τ_1 in all simulations, leading to a good agreement of experimental and simulated data. The drying potentials predicted by the drying model were used to calculate the coating layer porosities, which were then used in the simulations, with the correlations given in Figs. 8 and 11. The mass fraction of solid in the sprayed liquid w_s was set to be 0.3, as in the experiments. Furthermore, a property independent growth law was assumed, setting λ_2 in Eq. (18) to unity. The temperature of the sprayed liquid ϑ_{sus} was assumed to be 20 °C in all simulations.

In Figs. 16 and 17, the comparison between the measured and the simulated normalized particle size distribution for both experimental series is shown. The simulated distributions are in good agreement with the measured data.

5. Conclusion and outlook

In this work, fluidized bed coating experiments at different drying conditions were performed in a lab-scale plant to find a relationship between the porosity and the drying potential. Therefore, two different particle systems were used: non-porous glass beads and porous γ-alumina particles. After each experiment, samples were taken and the particle size distributions were measured. Additionally, scanning electron microscope images were produced and the porosity was determined by X-Ray micro-tomography measurements. For each particle system, a linear expression for the relationship between layer porosity and drying potential was obtained.

Further, a two compartment population balance model for fluidized bed coating with a new mathematical formulation for the growth kinetics including the porosity of the coating layer was presented. Since the porosity depends on the drying conditions, a heat and mass transfer model, providing the drying potential of the fluidization gas, was implemented as well. Simulations were performed with the obtained empirical correlations and compared with experimental data. The simulated particle size distributions show a good agreement with the measured ones in the case of non-porous glass beads and porous γ-alumina particles.

In this study it was shown, that the structure of coating layers depends strongly on the drying conditions. However, it is not clear, if the presented results and statements are valid in general, or only for the investigated materials. In order to gain more insight into the structure formation and to check the propositions made in this work, crystallization of sodium benzoate in droplets needs to be investigated experimentally at different drying conditions. Then, a more precise model, including e.g. the calculation of a crystal size distribution in a droplet, can be derived. Future work must also focus on testing the presented method with a non-crystallizing coating material. Further, possible droplet imbibition into porous structures has to be taken into account.

Notation

Symbols

A	Area	m²
A^*	Antoine constant	–
a	Parameter of a linear function	–
B^*	Antoine constant	°C
a	Parameter of a linear function	–
C^*	Antoine constant	°C
c	Specific heat capacity	J/(kg K)
d	Diameter	m
G	Growth rate	m/s
H	Enthalpy	J
$\dot{H}$	Enthalpy flow rate	J/s
Δh_{evap}	Specific enthalpy of evaporation at 0 °C	J/kg
L	Length	m
M	Mass	kg
$\dot{M}$	Mass flow rate	kg/s
n	Number density function	1/m
P	Pressure	Pa
q_0	Normalized number density function	1/m
$\dot{Q}$	Heat flow rate	W
t	Time	s
V	Volume	m³
w_s	Mass concentration of solid material in a liquid	–
x	Particle size	m
X	Moisture content (solid phase)	kg/kg
Y	Moisture content (gas phase)	kg/kg
z	Length coordinate	m

Greek symbols

α	Heat transfer coefficient	W/(m² K)
β	Mass transfer coefficient	m/s
ε	Porosity	m³/m³
ζ	Normalized spatial coordinate	–
η	Drying potential	–
ϑ	Temperature	°C
λ	Parameter of the growth kinetics	–
μ_j	j-th moment of size distribution	mʲ
ϱ	Mass density	kg/m³
τ	Residence time	s
φ	Relative size of the spray zone	–

Subscripts

1	Spray zone
2	Drying zone
bed	Fluidized bed
dry	Dry matter
evap	Evaporation
g	Gas
i	Initial condition
inlet	Inlet
outlet	Outlet
p	Particle
s	Solid
sat	Saturation
sh	Shell
sus	Solution (total)
sus, l	Solution (liquid)
sus, s	Solution (solid)
v	Vapor
w	Water

Acknowledgments

References

[1] S. Heinrich, M. Peglow, M. Ihlow, M. Henneberg, L. Mörl, Analysis of the start-up process in continuous fluidized bed spray granulation by population balance modelling, Chem. Eng. Sci. 57 (2002) 4369–4390.

[2] M. Hemati, R. Cherif, K. Saleh, V. Pont, Fluidized bed coating and granulation: influence of process-related variables and physicochemical properties on the growth kinetics, Powder Technol. 130 (2003) 18–34.

[3] P.D. Hede, P. Bach, A.D. Jensen, Batch top-spray fluid bed coating: scale-up insight using dynamic heat- and mass-transfer modelling, Chem. Eng. Sci. 64 (2009) 1293–1317.

[4] K. Terrazas-Velarde, M. Peglow, E. Tsotsas, Investigation of the kinetics of fluidized bed spray agglomeration based on stochastic methods, AIChE J. 57 (2011) 3012–3026.

[5] M. Dernedde, M. Peglow, E. Tsotsas, A novel, structure-tracking Monte Carlo algorithm for spray fluidized bed agglomeration, AIChE J. 58 (2012) 3016–3029.

[6] J. Li, B. Freireich, C. Wassgren, J.D. Litster, A general compartment-based population balance model for particle coating and layered granulation, AIChE J. 58 (2012) 1397–1408.

[7] A. Bück, E. Tsotsas, K. Sommer, Size enlargement, in: B. Elvers (Ed.), Ullmann's Encyclopedia of Industrial Chemistry, WILEY-VCH, 2014, pp. 1–47.

[8] R. Turton, Challenges in the modeling and prediction of coating of pharmaceutical dosage forms, Powder Technol. 181 (2008) 186–194.

[9] B. Guignon, A. Duquenoy, E.D. Dumoulin, Fluid bed encapsulation of particles: principles and practice, Dry. Technol. 20 (2002) 419–447.

[10] S.R.L. Werner, J.R. Jones, A.H.J. Paterson, R.H. Archer, D.L. Pearce, Air-suspension particle coating in the food industry: part I — state of the art, Powder Technol. 171 (2007) 25–33.

[11] K. Dewettinck, L. Deroo, W. Messens, A. Huyghebaert, Agglomeration tendency during top-spray fluidized bed coating with gums, Food Sci. Technol. 31 (1998) 576–584.

[12] M. Tzika, S. Alexandridou, C. Kiparissides, Evaluation of the morphological and release characteristics of coated fertilizer granules produced in a Wurster fluidized bed, Powder Technol. 132 (2003) 16–24.

[13] P.D. Hede, P. Bach, A.D. Jensen, Top-spray fluid bed coating: scale-up in terms of relative droplet size and drying force, Powder Technol. 184 (2008) 318–332.

[14] E. Tsotsas, Influence of drying kinetics on particle formation: a personal perspective, Dry. Technol. (2012) 1167–1175.

[15] F. Ronsse, J.G. Pieters, K. Dewettinck, Combined population balance and thermodynamic modelling of the batch top-spray fluidised bed coating process. Part 1: model development and validation, J. Food Eng. 78 (2007) 296–307.

[16] D.O. Silva, L.M. Tamiozzo, C.R. Duarte, V.V. Murata, M.A.S. Barrozo, Modeling of seed coating in a spouted bed, Dry. Technol. 29 (2011) 286–294.

[17] M. Dadkhah, M. Peglow, E. Tsotsas, Characterization of the internal morphology of agglomerates produced in a spray fluidized bed by X-ray tomography, Powder Technol. 228 (2012) 349–358.

[18] M. Dadkhah, Morphological Characterization of Agglomerates Produced in a Spray Fluidized Bed by X-ray Tomography(Ph.D. thesis) Otto-von-Guericke-Universität, Magdeburg, 2014.

[19] D.F. Sherony, A model of surface renewal with application to fluid bed coating of particles, Chem. Eng. Sci. 36 (1981) 845–848.

[20] P. Wnukowski, F. Setterwall, The coating of particles in a fluidized bed (residence time distribution in a system of two coupled perfect mixers), Chem. Eng. Sci. 44 (1989) 493–505.

[21] T. Hoffmann, M. Peglow, E. Tsotsas, Prozessdynamik der Wirbelschichtgranulierung, Chem. Ing. Tech. 83 (2011) 658–664.

[22] S.J. Maronga, P. Wnukowski, Modelling of the three-domain fluidized-bed particulate coating process, Chem. Eng. Sci. 52 (1997) 2915–2925.

[23] B.J. Ennis, G. Tardos, R. Pfeffer, A microlevel-based characterization of granulation phenomena, Powder Technol. 65 (1991) 257–272.

[24] N. Hampel, A. Bück, M. Peglow, E. Tsotsas, Continuous pellet coating in a Wurster fluidized bed process, Chem. Eng. Sci. 86 (2013) 87–98.

[25] L. Mörl, S. Heinrich, M. Peglow, Granulation, in: A.D. Salman, M.J. Hounslow, J.P.K. Seville (Eds.), Handbook of Powder Technology, Fluidized Bed Spray Granulation, vol. 11, Elsevier, 2007, pp. 21–188 (chap).

[26] M. Peglow, S. Antonyuk, M. Jacob, S. Palzer, S. Heinrich, E. Tsotsas, Particle formulation in spray fluidized beds, in: E. Tsotsas, A.S. Mujumdar (Eds.), Modern Drying Technology, Product Quality and Formulation, vol. 3, WILEY-VCH, 2011, pp. 295–378.

[27] S. Heinrich, M. Ihlow, M. Henneberg, M. Peglow, E. Machnow, L. Mörl, Studies of steam drying in a fluidized bed, Dry. Technol. 20 (2002) 175–194.

[28] H.G. Wang, T. Dyakowski, P. Senior, R.S. Raghavan, W.Q. Yang, Modelling of batch fluidised bed drying of pharmaceutical granules, Chem. Eng. Sci. 62 (2007) 1524–1535.

[29] M. Khanali, S. Rafiee, A. Jafari, S.H. Hashemabadi, Experimental investigation and modeling of plug-flow fluidized bed drying under steady-state conditions, Dry. Technol. 31 (2013) 414–432.

[30] M. Khanali, S. Rafiee, A. Jafari, Numerical simulation and experimental investigation of plug-flow fluidized bed drying under dynamic conditions, J. Food Eng. 137 (2014) 64–75.

[31] J. Burgschweiger, E. Tsotsas, Experimental investigation and modelling of continuous fluidized bed drying under steady-state and dynamic conditions, Chem. Eng. Sci. 57 (2002) 5021–5038.

[32] J. Richardson, W. Zaki, Sedimentation and fluidization: part I, Trans. Inst. Chem. Eng. 32 (1954) 35–53.

[33] H. Martin, VDI-Wärmeatlaschap Wärmeübergang in Wirbelschichten, Springer-Verlag, Berlin, Heidelberg, New York, 2006. Mf 1–Mf 9.

[34] B. Glück, Zustands- und Stoffwerte - Wasser, Dampf, Luft - Verbrennungsrechnung, Verlag für Bauwesen GmbH, Berlin, 1991.

[35] H. Groenewold, E. Tsotsas, Predicting apparent Sherwood numbers for fluidized beds, Dry. Technol. 17 (1999) 1557–1570.

[36] B. Koren, Numerical methods for advection–diffusion problemschap A Robust Upwind Discretisation Method for Advection, Diffusion and Source Terms, Vieweg, Braunschweig/Wiesbaden, 1993. 117–138.

[37] L.F. Shampine, M.W. Reichelt, The Matlab ODE Suite, SIAM J. Sci. Comput. 18 (1997) 1–22.

[38] L. Fries, S. Antonyuk, S. Heinrich, S. Palzer, DEM-CFD modeling of a fluidized bed spray granulator, Chem. Eng. Sci. 66 (2011) 2340–2355.

[39] M. Börner, M. Peglow, E. Tsotsas, Derivation of parameters for a two compartment population balance model of Wurster fluidised bed granulation, Powder Technol. 238 (2013) 122–131.